DOE/BC/95000168
(DE95000168)

FOAM FLOW THROUGH A TRANSPARENT ROUGH-WALLED ROCK FRACTURE

By
A. Kovscek, D. Tretheway, C. Radke, and P. Persoff

July 1995

University of California
Lawrence Berkeley Laboratory
Berkeley, California

Bartlesville Project Office
U. S. DEPARTMENT OF ENERGY
Bartlesville, Oklahoma

DOE/BC/95000168
Distribution Category UC-122

Foam Flow Through a Rough-Walled Rock Fracture

By
A. Kovscek, D. Tretheway,
C. Radke, and P. Persoff

July 1995

Prepared for
U.S. Department of Energy
Assistant Secretary for Fossil Energy

Thomas Reid, Project Manager
Bartlesville Project Office
P.O. Box 1398
Bartlesville, OK 74005

Prepared by
University of California
Lawrence Berkeley Laboratory
Berkeley, CA 94720

Foam Flow Through A Transparent Rough-Walled Rock Fracture

A. R. Kovscek, D. C. Tretheway, C. J. Radke
Earth Sciences Division of Lawrence Berkeley Laboratory
and Department of Chemical Engineering
University of California
Berkeley, CA 94720

P. Persoff
Earth Sciences Division of Lawrence Berkeley Laboratory
University of California
Berkeley, CA 94720

ABSTRACT

This paper presents an experimental study of nitrogen, water, and aqueous foam flow through a transparent replica of a natural rough-walled rock fracture with a hydraulic aperture of roughly 30 μm. It is established that single-phase flow of both nitrogen and water is well described by analogy to flow between parallel plates. Inertial effects caused by fracture roughness become important in single-phase flow as the Reynolds number approaches 1. Foam exhibits effective control of gas mobility. Foam flow resistances are approximately 10 to 20 times greater than those of nitrogen over foam qualities spanning from 0.60 to 0.99 indicating effective gas-mobility control.

Because previous studies of foam flow have focused mainly upon unfractured porous media, little information is available about foam flow mechanisms in fractured media. The transparency of the fracture allowed flow visualization and demonstrated that foam rheology in fractured media depends upon bubble shape and size. Changes in flow behavior are directly tied to transitions in bubble morphology.

Introduction

In fractured oil reservoirs, fracture networks provide flow paths with permeabilities several orders of magnitude larger than that of the unfractured reservoir matrix. Consequently, injected fluids flow preferentially through the fracture network slowing oil recovery. Gases and supercritical fluids commonly used for enhanced oil recovery (EOR) such as steam, carbon dioxide, and nitrogen have low viscosities and are especially prone to preferential channeling through fractures. If gas mobility can be controlled, oil displacement efficiency is improved.

Foam is a promising general agent for controlling gas mobility in EOR processes (Hirasaki 1989) and in other applications, such as aquifer storage of natural gas (Witherspoon *et al.* 1987) and compressed air. Aqueous foam is a dispersed gaseous phase within a continuous aqueous phase comprised mainly of thin films known as lamellae. The lamellae are stabilized by adsorption of surfactant at the gas/liquid interfaces. Foam exhibits large flow resistance and unusual rheological properties in unfractured, consolidated porous media (Persoff *et al.* 1991; Ettinger and Radke 1992). For example, Persoff *et al.* (1991) found that steady-state pressure drop and aqueous phase saturation were independent of gas velocity for a given liquid injection rate and linearly dependent on liquid velocity in a 1.2-μm^2 (1.2-Darcy) Boise sandstone.

Ettinger and Radke (1992) confirmed these results and also highlighted the role of foam texture and bubble shape in a 1-μm^2 Berea sandstone. They concluded that for foams generated *in situ*, foam bubbles are as large as pore bodies and that lamellae span the pores. Additionally, smaller bubbles (finer textured foams) cause a larger flow resistance (Ettinger and Radke 1992). Lamellae transport through fractures is similarly expected to cause large pressure drops.

Foams are classified according to their bubble size and gas volume fraction. In bulk foam the length scale of individual bubbles is much smaller than the characteristic length scale of the space confining the foam. Here, bubble shape is determined by the gas volume fraction of the foam. When the gas volume fraction is small, bubbles are roughly spherical and separated by thick lenses of aqueous liquid; this foam is denoted as kugelschaum ("ball foam"). Conversely, high gas volume fraction leads to polygonal bubbles or polyederschaum ("polyhedral foam"). Here, lamellae separate individual foam bubbles. On the other hand, when the characteristic length scale of individual bubbles is of the same

order or greater than the length scale of the pore space, foam is "confined" (Kovscek and Radke 1994). Foam lamellae or lenses completely span the pore space.

Before examining the flow of foam in a fracture, we review the forces responsible for flow resistance of confined foam in consolidated porous media. Generally, foam increases flow resistance in porous media by four mechanisms (Hirasaki and Lawson 1985; Falls *et al.* 1989): First, thin films of liquid between the foam bubbles and solid surfaces creates significant drag at the wall. This resistance occurs whether or not surfactant is present. Second, slugs of liquid and/or lamellae resist flow by creating drag at the wall. Third, a flowing bubble has an expanding interface at its leading end, thus depleting the interface in surfactant, and a contracting interface at its trailing end, with a corresponding enrichment of surfactant. The resulting gradient in surface tension opposes forward bubble motion and creates drag. Lastly, as lamellae flow, they pass through locations of irregular cross section requiring stretching and contraction. Not all of the work required to stretch a lamella is recovered. Viscous resistance to flow and interaction with nearby lamellae must consume a portion of this energy (Falls *et al.* 1989). The first three mechanisms act whether the confining surfaces are smooth or rough (*i.e.*, they act on flowing bubble trains in capillaries), while the fourth is operative in flow paths of varying aperture (Falls *et al.* 1989).

Our purpose is to understand the mechanisms of foam flow in fractures. A natural rock fracture is reproduced as a transparent replica, preserving its geometry. We choose a transparent fracture to observe whether foam in a fracture arrays itself as a confined foam or as a bulk foam. Furthermore, we wish to establish the rheological properties of foam in fractures. Although fracture flow in the subsurface environment is through networks of interconnected fractures, understanding flow in a single fracture is basic to understanding flow in fracture networks. Before describing the experimental apparatus, procedure, and results, the equations describing fracture flow are summarized.

Flow Equations

Currently, the most widely used equation describing fracture flow is derived by analogy to flow between smooth parallel plates (*c.f.*, (Schrauf and Evans 1986)). For creeping, radial flow of a Newtonian fluid,

$$-\frac{dp}{dr} = \frac{6\mu}{e^3 \pi r}\left(\frac{q_m}{\rho}\right) \qquad (1),$$

where the ratio of mass flow rate, q_m, to mass density, ρ, is the volumetric flow rate. Additionally, e is the aperture separating the plates, r is the radial distance from the origin, p is the pressure, and μ is the fluid viscosity. The aperture in Eq. 1 is cubed because the flow is proportional to both the permeability, which is quadratic in e, and the cross sectional area, which is proportional to e. For rough fractures, e is an effective hydraulic aperture; in a sense, it is the local aperture averaged over the ensemble of all possible flow paths. When fracture faces are rough, the aperture varies from point to point, and the hydraulic aperture does not necessarily equal the average geometric aperture (Schrauf and Evans 1986).

Equation 1 assumes that flow is laminar and inertial forces are negligible, and indicates that the pressure gradient increases linearly with flow rate. Deviations from linearity are observed in rough fractures at higher flow rates while still within the laminar regime. This behavior is reminiscent of viscous flow around single spheres (Batchelor 1988). For Reynolds numbers ($Re = \rho U d/ \mu$, where U is the free stream velocity and d the sphere diameter) near unity, Oseen (1910) demonstrated that inertial forces contribute an additional term to the drag force that is quadratic in velocity. By analogy, inertial losses are incorporated into Eq. 1 by adding a term that is proportional to the square of the velocity and is independent of fluid viscosity or

$$-\frac{dp}{dr} = \frac{6\mu}{e^3 \pi r}\left(\frac{q_m}{\rho}\right) + \frac{b}{4\pi^2 e^3 r^2}\frac{q_m^2}{\rho} \qquad (2),$$

where b is a dimensionless constant characteristic of the roughness.

The parallel-plate analogy is extended to the isothermal flow of an ideal gas (Schrauf and Evans 1986) by rewriting Eq. 1

$$-\frac{dp^2}{dr} = \frac{12\mu}{e^3 \pi \zeta r} q_m \qquad (3),$$

where ζ is a dimensional constant of proportionality between absolute pressure and the mass density of the ideal gas. Equation 3 teaches that the difference in the square of the

absolute pressure of an ideal gas increases linearly with mass flow rate when inertial forces are negligible. Equation 3 can be extended to nonlinear flow of an ideal gas in a manner similar to the construction of Eq. 2. A more detailed outline of these relations is given by Schrauf and Evans (1986).

Apparatus

Our experiments probe behavior at low flow rates (1 to 100 standard cubic centimeters per minute, SCCM, of nitrogen total throughput) in a radial system, whereas many previous experiments (Witherspoon *et al.* 1980; Schrauf and Evans 1986) with single-phase flow concentrated on higher rates (for instance, roughly 250 to 10,000 SCCM (Schrauf and Evans 1986)). We examine first the single-phase flow of nitrogen and water through a transparent replica of a rough-walled fracture. Then, we inject foam.

The experimental apparatus, shown schematically in Fig. 1, allows flow visualization, adjustment of fracture aperture, and measurement of pressure drop. It consists of a transparent epoxy fracture replica mounted horizontally between two pieces of Plexiglas (each 18.5 x 18.5 x 7.5 cm) with bolts for compressing the fracture located in each of the four corners of the block and 10 cm from the center. Nitrogen flows are metered by a Brooks mass flow controller (Brooks Instrument Division, Emerson Electric Co., Hatfield, PA). An ISCO Model 500D pump (ISCO Inc., Lincoln, NE) regulates liquid flows. Pressure is measured by a Heise Model C pressure gauge (Heise Bourdon Tube Company, Inc., Newtown, Conn.) for nitrogen flow and a Validyne model DP15 pressure transducer (Validyne Engineering Corp., Northridge, CA) for water and foam flow. Foam is formed either in the fracture itself or in a pregenerator made from a fired, 0.8-μm^2 Berea sandstone with a porosity of 0.24 that is encased axially in epoxy and measures 4.5 x 4.5 x 4.5 cm. A piece of 3.2 mm (1/8 in) metal tubing and a T junction prior to the injection point connects the fluid flow line and pressure transducer or gauge to the fracture replica.

The centerpiece of the apparatus is a 12-cm diameter, 2.5-cm thick cylindrical transparent replica of a natural rough-walled rock fracture. The original fracture is approximately perpendicular to the axis of a 12-cm diameter granite core from the Stripa mine, Sweden. Because granite is a hard, impermeable, crystalline rock, the fracture exhibits roughness length scales ranging from as large as a cm down to a few μm.

However, only roughness on the order of the fracture aperture (roughly 32 μm as shown in subsequent sections) or less is expected to contribute significantly to inertial losses.

Using the procedures and molds of Persoff *et al.* (1991), the replica was cast with Eccobond 27 clear epoxy (Emerson and Cumming, Dewey and Almy Chemical Division, W.R Grace Co., Canton, MA). The epoxy was cured for 24 hours at room temperature, further cured at 30° C for 12 hours, and then post-cured at 125° C for 3 hours. During the post-cure the epoxy changed from crystal clear to clear with an amber tint. Since weight gain suggested swelling in casts not subjected to the 125° C post-cure, the post-cured replica was submerged in water for 24 hours and weighed periodically to monitor any apparent swelling. No swelling or weight gain occurred. A drop of water wets a smooth sample of the post-cured epoxy with a 20° contact angle as measured by a contact-angle goniometer. A 2.0-mm diameter hole was drilled in the center of the upper half of the replica and used as the fluid injection point. The hole was widened halfway through to 3.2 mm (1/8 in), and a piece of 3.2-mm (1/8 in) stainless steel tubing was inserted from the top.

Foam is generated by coinjecting surfactant solution and nitrogen into the 0.8-μm^2 Berea-sandstone pregenerator or directly into the fracture. The foamer is a saline solution containing 0.83 wt% NaCl (Mallinckrodt Inc., Paris, KY) with 0.83 wt% active C_{14-16} α-olefin sulfonate (Stepan Bioterge AS40, Stepan Company, Anaheim, CA). The water was deionized and filtered before use. Solution surface tension and viscosity are 33 mN/m (Wilhelmy plate method) and 1.0 mPa·s, respectively.

Results

Flow Characterization of Fracture

The fracture replica was assembled and mounted between the two Plexiglas blocks, as illustrated in Fig. 1. A battery of preliminary experiments were done to characterize the fracture, to select the appropriate torque for compressing the fracture, and to confirm reproducibility of measurements when the fracture was disassembled and reassembled.

First, the fracture was assembled, the bolt torque set at 18.1 N·m, and nitrogen gas flowed through the fracture at a stepwise increasing rate. The linear relation between pressure drop squared and mass flow rate in Fig. 2 demonstrates that the inertial contribution for gas flow is negligible at mass flow rates less than 2 mg/s of nitrogen. The

Reynolds number calculated at the fracture outlet (using e as the characteristic dimension) for the highest flow rates is less than 0.3.

Next, measurements were made at several levels of bolt torque. The integrated form of Eq. 3 determines the effective aperture from data such as those displayed in Fig. 2. The torque on each bolt was increased uniformly beginning from 9.04 N·m until further torquing produced no change in the effective aperture, as demonstrated in Table 1. No hysteresis was observed as torque was varied from low to high to low. A torque of 18.1 N·m was chosen for all subsequent experiments.

The second set of experiments determined whether the fracture could be disassembled and retain reproducible flow properties. The fracture was disassembled and reassembled several times and the pressure-drop response for both water and nitrogen recorded. For nitrogen flow, the closed diamonds in Fig. 2 indicate the excellent reproducibility of the flow data after reassembly of the fracture. Also, Table 2 reports the reproducibility of the fracture aperture for the disassembly-reassembly operation.

For water (and later for foam) runs, we assembled the fracture under water. This eliminated air bubbles in the fracture. The four bolts securing the Plexiglas were then tightened incrementally and equally to the desired torque. To obviate capillary end effects in the water and foam experiments, the fracture was kept submerged in water and the water level maintained just even with the fracture.

Figure 3 graphs the pressure drop versus flow rate data for water and again shows the excellent reproducibility upon fracture reassembly. Different symbols on the figure again indicate that the fracture was disassembled between experimental runs. Since the plot of pressure drop versus mass flow rate in Fig. 3 is parabolic passing through the origin, inertial losses are significant for water flow. Re at the fracture outlet is roughly 2 at the largest flow rates. The onset of inertial effects caused by fracture roughness occurs when Re is of order 1 as suggested earlier by the analogy to Oseen flow. When Re is much less than unity no inertial losses are found.

For water flows, the effective aperture is found by first integrating Eq. 2 and then dividing both sides by q_m. When $\Delta p/q_m$ versus q_m is plotted, the intercept is proportional to e^{-3}. Apertures obtained from water flow are shown in Table 2. These data demonstrate that fracture reassembly is reproducible and that the same aperture is calculated for both water and nitrogen flow (Table 2).

Upon completion of the above battery of experiments, the single rough fracture is well characterized. Under a torque of 18.1 N·m per bolt the fracture is compressed to an

aperture of 32 μm, and the fracture apparatus can be assembled and disassembled reproducibly. Inertial effects are only important when Re is of order unity. In the next section, we explore foam morphology and flow behavior.

Flow Visualization

Since the rheology of foam is strongly tied to foam texture, we observed foam bubble shape and size in all experiments. As a first step in flow visualization, dyed water was injected (Liquitint Patent Blue, Chemcentral, Romulus, MI) at the fracture inlet to observe the single-phase flow of water via a video camera mounted normal to the fracture. Water flowed primarily radially outward; no regions of gross water channeling were seen.

Second, the effect of injection rates on effluent bubble size from the Berea-sandstone pregenerator was noted. Ettinger (1989) measured effluent bubble-size distributions from this pregenerator and found bubble diameters of 100 to 400 μm at room temperature and pressure in a flow-rate range similar to that employed in this work. Bubble size increased with increasing gas flow rate and decreased with increasing liquid flow rate. Our observations confirmed the effects of flow rate on bubble size described above. This liquid-rate behavior can be interpreted as meaning that the frequency of liquid lens formation by snap-off and subsequent drainage to a lamella is limited by the ability of the porous medium to deliver liquid to snap-off sites. Higher liquid rates leads to more numerous lamellae and smaller bubbles. Larger gas flow rates result in more lamellae coalescence and larger bubbles.

The transparency of the fracture permitted direct observation of the *in-situ* foam texture. For exit gas fractional flows, f_g, from 0.61 to almost unity, two different types of foam morphology emerged. In cross section, as shown in Figs. 4a and 5a, gas bubbles elongate and span the aperture. However for f_g above about 0.97, Fig. 4a indicates that lamellae separate the bubbles and in plan view (Fig. 4b) the bubbles are polygonal. Below an exit f_g of 0.9, bubbles were generally circular in plan view and separated by thick aqueous lenses as shown in Fig. 5. Both of these arrangements are referred to as bulk two-dimensional foam (Princen 1983). At intermediate exit f_g values, bubbles entered the fracture as circles in plan view and expanded as they flowed outward to assume a polygonal shape (generally hexagonal).

Pregenerated foam did not coalesce when injected into the fracture, nor were additional foam lenses or lamellae generated. Individual foam bubbles maintained their identity as they flowed through the fracture. However, bubble expansion was observed.

Bubble volume increased two to fourfold, consistent with the pressure drop decline, as foam moved outward through the fracture. Foam lamellae or lenses were generally more densely spaced than the largest roughness protrusions (Figs. 4a and 5a).

Similar to single-phase water flow in the fracture, foam at steady state did not selectively channel. However, in the polygonal configuration, foam flow alternated sporadically among several different paths. In the circular configuration, foam flowed continuously everywhere in the fracture, although bubbles did move more rapidly in one particular sector.

Foam was also generated by injecting nitrogen and surfactant solution directly into the fracture. The primary foam generation mechanism appeared to be capillary snap-off similar to that in unfractured porous media (Chambers and Radke 1991). The average bubble size, though, of the *in-situ* generated foam was roughly 4 times larger than foam generated by the 0.8-μm^2 Berea sandstone pregenerator. This result is expected because of the smaller number of snap-off sites (Chambers and Radke 1991) (*i.e.*, pore-body and pore-throat connections with an aspect ratio greater than about 2) in the fracture compared to that in the sandstone.

Foam Flow

Three foam injection schemes were used. First, the liquid surfactant solution injection rate was held constant while the nitrogen flow rate was varied from 10 to 200 $\mu g/s$ (approximately 0.5 to 10 SCCM). Next, the nitrogen injection rate was fixed and the surfactant solution injection rates adjusted from 0.2 to 20 mg/s (0.02 to 2.0 cm^3/min). Finally, the ratio of gas and liquid flow rates was held constant and the total mass flow rate increased. Foam was both pregenerated in the 0.8-μm^2 Berea sandstone pregenerator and *in situ*. For all injection schemes, thirty to sixty minutes were needed for the pressure drop to stabilize after each change in flow rate.

Figure 6 reports a linear pressure-drop response when pregenerated foam was injected into the fracture while foamer solution rate was held constant and the gas rate increased. Three different constant liquid rates are plotted: 1.67, 4.17 and 6.72 mg/s. Gas fractional flows, f_g, computed at exit conditions, are listed in parentheses next to individual data points and span from 0.81 to 0.98. Although bubble expansion is observed visually, the pressure-drop response indicates that foam behaves, apparently, as an incompressible fluid in this mode of injection. The solid lines, which are merely drawn through the data points to guide the reader's eyes, do not pass through the origin, suggesting an apparent

yield stress. A striking feature of Fig. 6 is lower pressure drop with increasing liquid flow at a given gas rate. Individual runs are very repeatable (triangular and circular symbols at 4.17 mg/s of liquid injection indicate separate experimental runs) and no hysteresis is evident (dark circles were obtained when gas flow was decreasing).

It is useful to express results via a mobility reduction factor (MRF). Integration and rearrangement of Eq. 1 indicates that the volumetric flow rate (at exit conditions) divided by the product of pressure drop and $2\pi e$ describes gas mobility. MRF is then obtained as the ratio of mobilities for foam and single-phase flow of nitrogen at identical volumetric gas flow rates. Here, an average MRF is defined by the ratio of pressure drops across the fracture,

$$\text{MRF} \equiv \frac{\Delta p_f}{\Delta p_g} \qquad (4),$$

where the subscript g denotes single-phase gas flow and the subscript f denotes foam. It is clear that foams with large flow resistance must display a large MRF.

For a volumetric flow rate of 0.15 cm^3/s at STP or roughly 180 μg/s of nitrogen, the MRF at a liquid injection rate of 4.17 mg/s is 21. Likewise, the MRF is 15 when the liquid rate is 6.72 mg/s. In this mode of injection, nitrogen flow resistance is substantially increased by segregation into the foam.

Next, the aqueous surfactant flow rate was varied at a given nitrogen flow rate. Fig. 7 gives results for pregenerated foam at three different gas rates: 96.3, 75.6, and 53.2 μg/s. The results reported in Fig. 7 are dramatically different from those in Fig. 6. Focusing on the nitrogen flow rate of 75.6 μg/s, three different flow regimes are found. In the first regime between flow rates of zero and approximately 2 mg/s (f_g = 0.97), the pressure drop increases approximately linearly to 180 kPa where it peaks. In the second regime, the pressure drop decreases from the maximum to roughly 140 kPa between liquid rates of 2 mg/s and 5 mg/s (f_g = 0.94). In the final regime, pressure drop is roughly constant at 140 kPa for flow rates above 5 μg/s. Results shown for the other two constant nitrogen rates also indicate these three flow regimes. Again the measurements are highly repeatable (different symbols indicate separate experiments), and there is no hysteresis. However, to move from a steady state at high liquid flow rate to steady state at a lower liquid flow rate requires several hours. Fig. 7 indicates MRF's of 10 to 20.

In the last mode of fluid injection, gas fractional flow was held constant but the total flow rate was increased. The gas fractions or qualities shown are again calculated at exit conditions. Fig. 8 labels the abscissa as water flow rate rather than total mass flow rate because nitrogen adds little to the overall mass flow rate. Foams flowing at 95% quality produce the largest pressure drop and as quality decreases so does the pressure drop. Here, pressure drop increases linearly as the total flow rate increases. Again, an apparent nonzero intercept is found. Also contrasted are pressure drops for *in-situ* generated and pregenerated foam. *In-situ* generated foam yields pressure drops about one-half the value of the pregenerated foam. Interestingly, the pressure drop for *in-situ* generated foam increases linearly with a slope almost identical to pregenerated foam of the same quality. Moreover, the linear increase in pressure drop with flow rate for a given quality in Figure 8 is reminiscent of incompressible fluids with a constant shear viscosity.

The generality of the results presented in Figs. 2 through 8 were verified by repeating the above experiments in a second transparent fracture replica that had an aperture of approximately 100 μm (Kovscek 1994).

Discussion

The results of Figs. 6 and 7 are counterintuitive. The pressure drop decreases as liquid rate is increased at a fixed gas rate in both figures. However, this finding can be understood by considering bubble morphology and its effect on flow resistance. Essentially, low quality foam is more mobile than high quality foam because of the availability of liquid to lubricate the rough fracture surfaces. We proceed by first explaining the observed bubble shapes and then consider the mobility of foam in fractures.

Flow visualization demonstrates that each foam bubble is confined vertically by the rough fracture walls, but laterally each bubble is confined only by other bubbles. Thus, foam inside the fracture is in a bulk two-dimensional configuration, as illustrated in Figs. 4b and 5b. Princen (1983) examined bulk two-dimensional foams theoretically, and showed that a transition in bubble morphology from polyederschaum (polyhedral) to kugelschaum (spherical) foam must occur at a gas fraction of 0.9069 assuming infinitely thin lamellae. At lesser gas fractions, capillary suction pressure is low, the Plateau borders cannot hold all of the liquid present, lamellae cannot form, and foam appears circular or kugelschaum in plan view.

In our experiments, the bubble shape begins to shift from two-dimensional polyederschaum to kugelschaum at an f_g of roughly 0.97, when the gas fractional flow is computed at exit conditions. If gas fractional flow at the inlet rather than the outlet is computed, we find that the transition in bubble shape starts at an f_g of approximately 0.92, which corresponds closely to the theoretical transition predicted by Princen (1983). Because of gas compressibility, bubbles expand as they flow toward the exit obviating all bubbles from changing from two-dimensional polyederschaum to kugelschaum throughout the fracture. Therefore, both bubble shapes are flowing over a range of fractional flows.

At high qualities (*i.e.*, $f_g \geq 0.97$) when the foam is polyhedral, most of the liquid volume is held in the Plateau borders because the capillary-suction pressure is large. As a result, not only are the lamellae separating bubbles thin, but so are the films coating the solid surface (Hirasaki and Lawson 1985). Fluid resistance in thin wetting films is inversely proportional to the local film thickness cubed, inhibiting appreciable transport of wetting liquid through thin films. Additionally, at high foam qualities little bulk liquid resides in the network of nooks, crannies, and corners that compose the fracture roughness. Conversely, at low qualities, the ample liquid content of the foam allows lenses to form between bubbles and fill in the surface roughness.

Due to the complex mechanisms of foam transport and the geometry of the rough fracture, the foam flow here is not treated exactly. We can, however, understand most of the behavior in Figs. 6 and 7 by considering the components of foam flow that contribute significantly to flow resistance. Foam-flow resistance in rough fractures arises primarily because a flowing bubble must lay down a thin lubricating liquid layer on the fracture wall and liquid slugs between bubbles encounter drag at the fracture surface. Additionally, the pressure drop that drives foam bubbles also drives wetting aqueous liquid flow through the interconnected nooks and crannies of the fracture roughness. Thus, the fracture roughness has a strong effect on foam flow.

Since the gas bubbles are inviscid compared to the foamer solution, a no-stress interface between the gas and liquid is assumed. Thus, the flow of wetting liquid in the corners of the roughness and the bubble flow are decoupled, and we may discuss separately the pressure-drop effects of liquid flow in the fracture roughness network and foam-bubble flow. These separate analyses should yield consistent results. First, the results of Fig. 7 are discussed, where the liquid flow rate was increased while the gas velocity was held constant. Next, the linear pressure-drop response to increasing gas velocity at a constant liquid rate in Fig. 6 is considered.

Ransohoff and Radke (1988) analyzed the unidirectional flow of wetting liquid along the corners of noncircular capillaries and determined that the volumetric flow rate, q_c, scales linearly with the axial pressure gradient:

$$q_c = \frac{A_c a^2}{\beta \mu_w}\left(-\frac{dp}{dr}\right) \qquad (5),$$

Here, A_c is the cross-sectional area of wetting liquid occupying the corner, a is the circumferential radius of curvature of the gas-liquid interface, μ_w is the wetting liquid viscosity, and β is a dimensionless flow resistance that depends on the corner geometry and the gas-liquid contact angle. β decreases drastically as the contact angle approaches zero (Ransohoff and Radke 1988). Ransohoff and Radke also find that the presence of a no-slip interface only increases β by a factor of roughly two.

Integration of Eq. 5 reveals that the pressure drop scales linearly with liquid flow rate as long as A_c and a are constant. This is the experimental result found in Fig. 7 for gas fractional flows greater than 0.97. As f_g decreases further, the two-dimensional foam changes from polyederschaum to kugelschaum. Consequently, the cornered roughness begins to fill with wetting liquid, increasing the radius of interfacial curvature. Hence, the product of A_c and a^2 increases, and the pressure drop declines as reported in Fig. 7. The region of decline in pressure drop with increasing liquid flow rate corresponds to the range of foam qualities where both polyederschaum and kugelschaum two-dimensional foam are present in the fracture.

Once kugelschaum foam fills the fracture, the gas/liquid interfacial curvature is fixed by the semi-spherical endcaps that encompass foam bubbles (Fig. 5a). A_c and a^2 again become constant. To accommodate further increases in the volumetric liquid flow at a fixed gas rate, the liquid slugs separating foam bubbles lengthen. Since the fractional flow of gas is large, the gas injection rate mostly sets the superficial velocity of bubbles. Although the liquid slug size is increased slightly, the drag contribution from slugs is not appreciably larger. Slug velocity is nominally constant in this mode of injection, where the liquid rate is increased at a constant gas injection rate. The integrated form of Eq. 5 teaches that since $q_c/A_c a^2$ is constant, the macroscopic pressure drop should become sensibly independent of liquid flow rate at a given gas rate .

Foam bubble flow resistance explains the flow-rate trends with increasing gas velocity reported in Figs. 6 and 7. The effective viscosity, or equivalently flow resistance,

arising from flowing bubbles depositing thin liquid films on fracture walls scales as $n_f/Ca^{1/3}$, where n_f is the bubble texture or number of bubbles per unit volume, and Ca ($=U_g\mu_w/\sigma$) is the capillary number(Hirasaki and Lawson 1985; Falls *et al.* 1989). The proportionality constant here, in part, depends on the fracture cross-sectional geometry and the interfacial curvature of the gas-liquid interface (Hirasaki and Lawson 1985; Wong *et al.* 1993). The resistance arising from lens flow scales as $\mu_w L_s n_f$, where L_s is the lens or slug length (Hirasaki and Lawson 1985; Falls *et al.* 1989). We neglect the resistance for bubbles to slip past each other and for lamellae to stretch and contract as they encounter varying apertures along their flow path. Also, because the surface tension gradient encountered by a flowing surfactant-laden bubble generally increases flow resistance, but does not change the flow rate dependence of the flow resistance (Hirasaki and Lawson 1985), we neglect the surface tension gradient while retaining the predicted flow-rate dependence. This last simplification is consistent with our assumption of a no-stress interface between the gas bubble and the liquid-filled cornered roughness.

The overall effective viscosity for bubble flow in our fracture is the sum of the above terms, $\alpha_1 n_f/U_g^{1/3} + \alpha_2 L_s n_f$. The proportionality constant, α_1, combines fluid properties, such as liquid viscosity and surface tension with interfacial curvature, whereas, α_2 combines liquid viscosity and fracture surface area. These flow resistances are formally substituted into Eq. 1 to read

$$-\frac{dp}{dr} = \frac{12}{e^2}\left(\frac{\alpha_1 n_f}{U_g^{1/3}} + \alpha_2 L_s n_f\right) U_g \qquad (6),$$

where the volumetric flow rate, q_m/ρ, has been converted to velocity, U, with division by cross-sectional area, $2\pi re$. Since the volumetric gas injection rate is large compared to the liquid rate, *i.e.*, $q_{mg}/\rho_g >> q_{mw}/\rho_w$, the local bubble velocity, U_g, sets the pressure drop in Eq. 6. The subscripts mw and mg refer to the mass injection rates of foamer solution and gas, respectively.

The pregenerator supplies foam with a texture that scales with superficial gas and liquid velocity (Ettinger 1989; Ettinger and Radke 1992) as $U_w/U_g^{2/3}$, where the proportionality constant sets the absolute size of the foam bubbles. No foam coalescence inside the fracture was witnessed. Thus, this scaling is substituted directly for the *in-situ* foam texture in Eq. 6 to read

$$-\frac{dp}{dr} = \frac{12}{e^2} U_w \left(\alpha_3 + \alpha_4 L_s U_g^{1/3}\right) \qquad (7).$$

Eliminating the velocities in favor of the experimentally measurable quantities, q_{mg}, q_{mw}, p, and r and then integrating, we find that

$$-\Delta p = \frac{12}{e^3} q_{mw} \left[\alpha_5 \ln\left(\frac{R_2}{R_1}\right) + \int_{R_1}^{R_2} \frac{\alpha_6 L_s \, q_{mg}^{1/3}}{(e\,p)^{1/3}\, r^{4/3}} dr \right] \qquad (8)$$

where the superficial velocities and the mass flow rates are interrelated through the expression $q_{mi} = 2\pi r e \rho_i U_i$. R_1 and R_2 refer to the inner and outer radii of the fracture and the proportionality constants α_5 and α_6 combine the aqueous phase fluid properties with flow resistance, foam texture, and ideal gas proportionality constants.

The first term inside the brackets of Eq. 8 is independent of gas flow rate and is the source of the apparent yield stress in Fig. 6 where gas flow rates are adjusted while the liquid injection rate is held constant. Note that there is no apparent yield stress when liquid injection rate is adjusted at a constant gas rate. The second term is not linearly proportional to the gas mass flow rate, but does correctly predict that the pressure drop should increase with gas flow rate at a fixed q_{mw}, as shown in Figs. 6 and 7. Further, because of the scatter in data points and because the gas mass flow rates reported in Fig. 6 are quite low, it is hard to distinguish between a linear or a weakly curved 1/3-power velocity dependence.

In agreement with the previous discussion of Eq. 5, Eq. 8 predicts that the pressure drop should increase almost linearly with liquid rate at high gas fractional flows. For a constant gas rate and constant α_3 and α_4 obtained at high gas fractional flows, the term in the brackets on the right of Eq. 8 is nearly constant. However, as the bubble curvature decreases so do the proportionality constants for flow resistance. Again, this predicts that the pressure drop should decrease with increasing liquid injection rates in the transition region from two-dimensional polyederschaum to kugelschaum foam as found in both Figs. 6 and 7.

Equation 8 also explains why the pressure drops for *in-situ* generated foam are less than the pregenerated foam. The proportionality constants, $\alpha_{3,4}$, include information about the size of the foam bubbles. Because foams formed *in situ* are coarser than the pregenerated foam, $\alpha_{3,4}$ are smaller and the pressure drop is less for the *in-situ* generated

foams. However, the flow-rate dependence and scaling of texture with gas and liquid injection rates remains identical for both pregenerated and *in-situ* generated foams.

Conclusions

Continuous nitrogen and water flow through a transparent replica of a natural rough-walled rock fracture with an average aperture of 30 μm, is well described by the parallel-plate model. Inertial effects caused by wall roughness become important in single-phase flow as Re approaches 1.

Visual observation reveals that foam in fractures arrays itself as a bulk two-dimensional foam. Lamellae bridge the fracture aperture at high foam qualities. A transition in foam bubble shape from polyhedral to spherical occurs near the theoretically predicted foam quality of 0.91. Maximum flow resistance occurs near this transition. Foam with thin lamellae separating gas bubbles and thin films coating solid surfaces exhibit a larger flow resistance than do foams with thick liquid lenses separating foam bubbles and thick wetting films coating fracture surfaces. The shape and texture of foam bubbles in the plane of the fracture controls foam rheology.

Foam effectively reduces gas mobility in fractures. Mobility reduction factors (MRF) of 10 to 20 are found for foam flow. That is, dispersing gas as foam in fractures increases gas flow resistance 10 to 20 times. The rheology of foam in fractures is complicated. The range of flow rates examined in these experiments revealed three flow regimes. First, at gas fractional flows above 0.97, the pressure drop is proportional to the liquid flow rate at a fixed gas flow rate, and *vice versa*. Second, for gas fractional flows below roughly 0.9, the pressure drop is insensitive to liquid flow rate, but increases linearly with gas flow rate. Third, at intermediate gas fractional flows where both polyederschaum and kugelschaum foam flow through the fracture, the pressure drop actually decreases with increasing liquid flow rate.

Above an apparent yield stress, foam flow in fractures exhibits a shear-rate-independent flow resistance when the gas velocity is increased while the liquid velocity is fixed, and also, when the total mass flow rate is increased while holding the quality constant. The apparent yield stress exhibited in these modes of fluid injection is well explained by incorporating an effective foam viscosity into the classical parallel-plate fracture equations. Finally, the transition region where pressure drop decreases with

increasing liquid injection (and decreasing foam quality) is understood because flow resistance decreases as the gas/liquid interfacial curvature decreases.

Acknowledgment

This work was supported by the Assistant Secretary for Fossil Energy, Office of Oil, Gas, and Shale Technologies of the U.S. Department of Energy under Contract No. DE-AC03-76FS00098 to the Lawrence Berkeley Laboratory of the University of California.

Nomenclature

a	radius of interfacial curvature
A_c	cross-sectional area occupied by wetting liquid
b	dimensionless coefficient characterizing the effect of roughness
Ca	capillary number, dimensionless ratio of viscous to interfacial forces
d	characteristic dimension in the Reynolds number
e	hydraulic fracture aperture
L_s	length of a liquid slug
n_f	foam texture or number of bubbles per unit volume
p	pressure, absolute pressure
MRF	dimensionless mobility reduction factor
q	flow rate, mass or volumetric
r	radial distance
R	denotes inner or outer radii of the fracture
Re	Reynolds number, dimensionless ratio of inertial to viscous forces
U	bubble or gas velocity
v	linear velocity appearing in the Reynolds number

Greek Symbols

α	proportionality constants for flow resistance
β	dimensionless corner flow resistance for wetting liquid
μ	viscosity
ρ	density
ζ	proportionality constant between pressure and ideal gas density

Subscripts

c	corner flow
f	foam
g	gas
m	mass flow rate
w	wetting liquid

References

Batchelor, G. K., 1988. An Introduction to Fluid Dynamics. Cambridge University Press, Cambridge.

Chambers, K. T. and Radke, C. J., 1991. Capillary Phenomena in Foam Flow Through Porous Media. In: Morrow, N. R. (Editor). Interfacial Phenomena in Petroleum Recovery. Marcel Dekker Inc., New York, pp 191-255.

Ettinger, R. A., 1989. Foam Flow Resistance in Berea Sandstone. M.S. thesis University of California, Berkeley.

Ettinger, R. A. and Radke, C. J., 1992. Influence of Texture on Steady Foam Flow in Berea Sandstone. Soc. Pet. Eng. Res. Eng. **7**(1): 83-90.

Falls, A. H., Musters, J. J. and Ratulowski, J., 1989. The Apparent Viscosity of Foams in Heterogeneous Beadpacks. Soc. Pet. Eng. Res. Eng. **4**(2): 155-164.

Hirasaki, G. J., 1989. The Steam Foam Process. J. Petr. Tech. **41**(5): 449-456.

Hirasaki, G. J. and Lawson, J. B., 1985. Mechanisms of Foam Flow in Porous Media: Apparent Viscosity in Smooth Capillaries. Soc. Pet. Eng. J. **25**(2): 176-190.

Kovscek, A. R., 1994. Foam Displacement in Porous Media: Experiment and Mechanistic Prediction by the Population Balance Method. Ph. D. thesis University of California, Berkeley.

Kovscek, A. R. and Radke, C. J., in press 1994. Fundamentals of Foam Transport in Porous Media. In: Schramm, L.L. (Editor). Foams: Fundamentals and Applications. American Chemical Society, Washington D. C.

Oseen, C. W., 1910. Über die Stokessche Formel und über eine verwandte Aufgabe in der Hydrodynamic. Arkiv Math. Astro. Fys. **6**(29).

Persoff, P., Pruess, K. and Meyer, L., 1991. Two-Phase Flow Visualization and Relative Permeability Measurement in Transparent Replicas of Rough-Walled Rock Fractures. 16th Workshop on Geothermal Reservoir Engineering, Stanford, University,

Persoff, P., Radke, C. J., Preuss, K., Benson, S. M. and Witherspoon, P. A., 1991. A Laboratory Investigation of Foam Flow in Sandstone at Elevated Pressure. Soc. Pet. Eng. Res. Eng. **6**(3): 365-371.

Princen, H. M., 1983. Rheology of Foams and Highly Concentrated Emulsions. J .Colloid and Interface Sci. **91**(1): 160-175.

Ransohoff, T. C. and Radke, C. J., 1988. Laminar Flow of a Wetting Liquid along the Corners of a Predominantly Gas-Occupied Noncircular Pore. J. Coll. Interface Sci. **121**(2): 392-401.

Schrauf, T. W. and Evans, D. D., 1986. Laboratory Studies of Gas Flow Through a Single Natural Fracture. Wat. Resour. Res **22**(7): 1038-1050.

Witherspoon, P.A., Radke, C.J., Shikari, Y., Pruess, K., Persoff, P., Benson, S.M. and Wu, Y.S., 1987. Feasibility Analysis and Development of Foam-Protected Underground Natural Gas Storage Facility (LBL-23500). American Gas Association, Proceedings Operating Section, paper #87-DT-110, pp 539-549.

Witherspoon, P. A., Wang, J. S. Y., Iwai, K. and Gale, J. E., 1980. Validity of a Cubic Law for Fluid Flow in a Deformable Rock Fracture. Wat. Resour. Res. **16**(6): 1016-1024.

Wong, H., Radke, C. J. and Morris, S., submitted 1993. The Motion of Long Bubbles in Polygonal Capillaries: II. Drag, Fluid Pressure, and Fluid Flow. J. Fluid Mechanics.

TABLE 1

Bolt-Torque Dependence of Aperture for Single-Phase Flow of Nitrogen

Torque per bolt (N·m)	Aperture (μm)
9.04	33.9
13.6	32.9
18.1	32.0
20.3	31.8

TABLE 2

Reproducibility of Single-Phase Flow Experiments,
Torque = 18.1 N·m/bolt

Fluid	Aperture (μm)
nitrogen	32.0
	31.7
	31.9
water	31.0
	30.9

Figure Captions

Figure 1: Schematic of experimental flow system

Figure 2: Square of steady-state pressure drop versus nitrogen mass flow rate in a fracture with a hydraulic aperture of roughly 30μm. Squares and diamonds indicate separate experimental runs including fracture reassembly.

Figure 3: Steady state pressure drop versus mass flow rate of water in a fracture with a hydraulic aperture of roughly 30 μm. Squares and diamond indicate separate experimental runs including reassembly of the fracture.

Figure 4: Foam morphology inside a transparent replica of a fracture at high gas volume fraction: (a) Lamellae span the fracture aperture (b) plan view of foam bubble shape

Figure 5: Foam morphology inside a transparent replica of a fracture at low gas volume fraction: (a) Aqueous lenses span the fracture aperture (b) plan view of foam bubble shape

Figure 6: Steady-state pregenerated foam pressure drop versus nitrogen flow rate at three different constant liquid rates. Circles and squares indicate separate experimental runs. Straight lines are drawn to guide eyes. Numbers in parentheses indicate the exit gas fractional flow.

Figure 7: Steady state pregenerated foam pressure drop versus aqueous phase flow rate at constant nitrogen mass injection rate. Different symbols indicate separate experimental runs. Lines connect data points. Numbers in parentheses indicate the exit gas fractional flow.

Figure 8: Steady state pressure drop for pregenerated and *in-situ* generated foam versus aqueous phase flow rate. Foams are of constant exit quality. Straight lines are drawn to guide eyes.

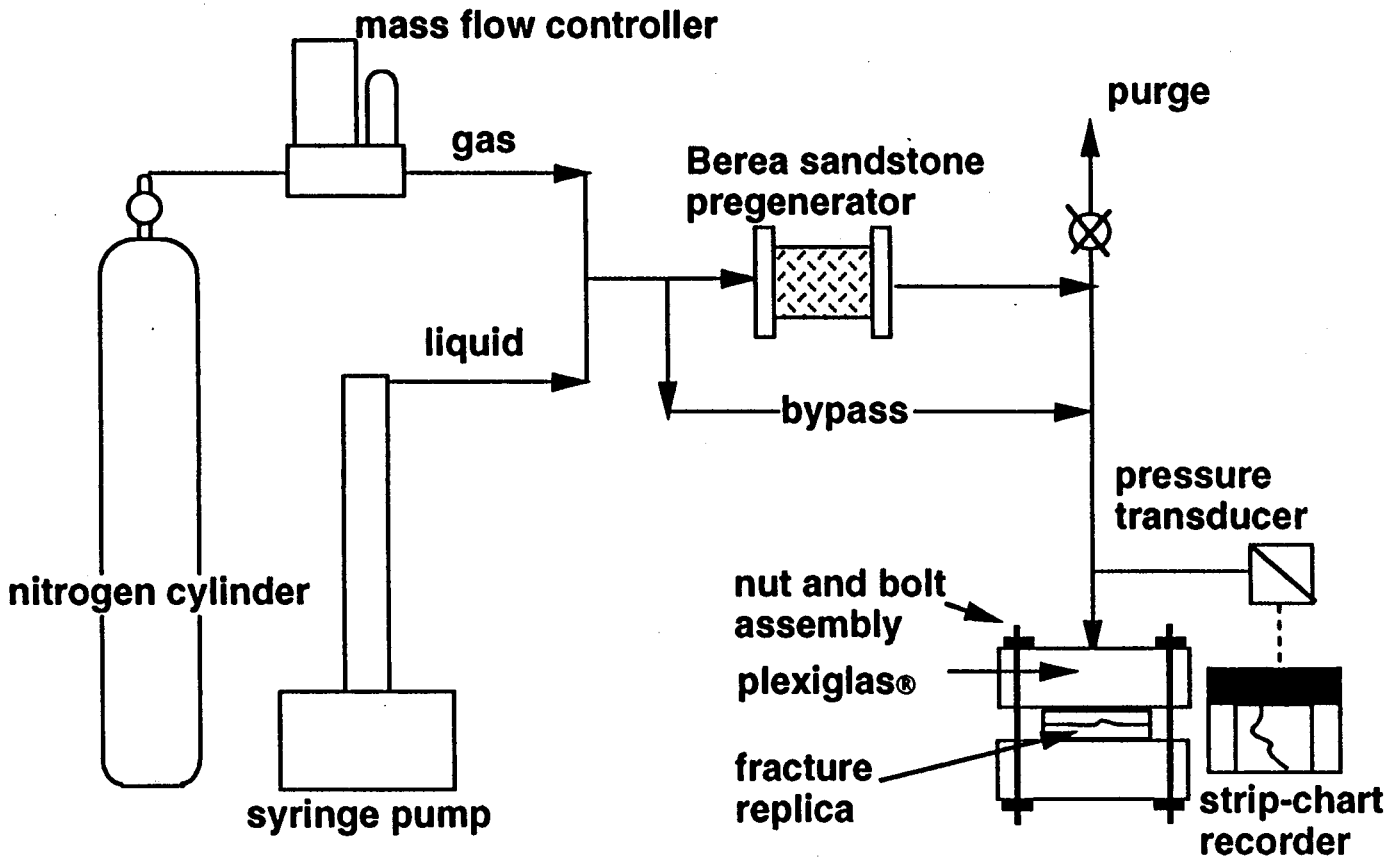

Fig. 1 Kovscek, Tretheway, Persoff, and Radke

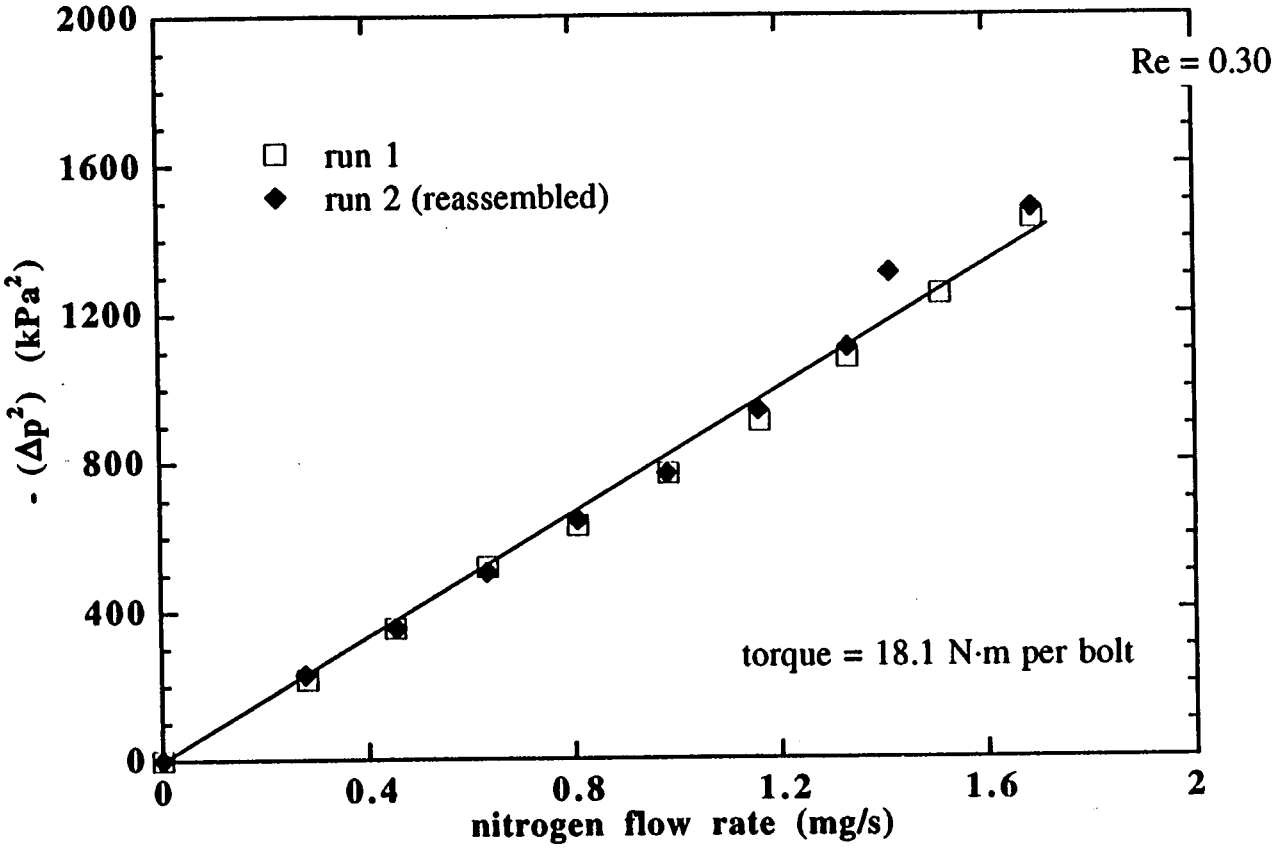

Fig. 2:Kovscek, Tretheway, Persoff, and Radke

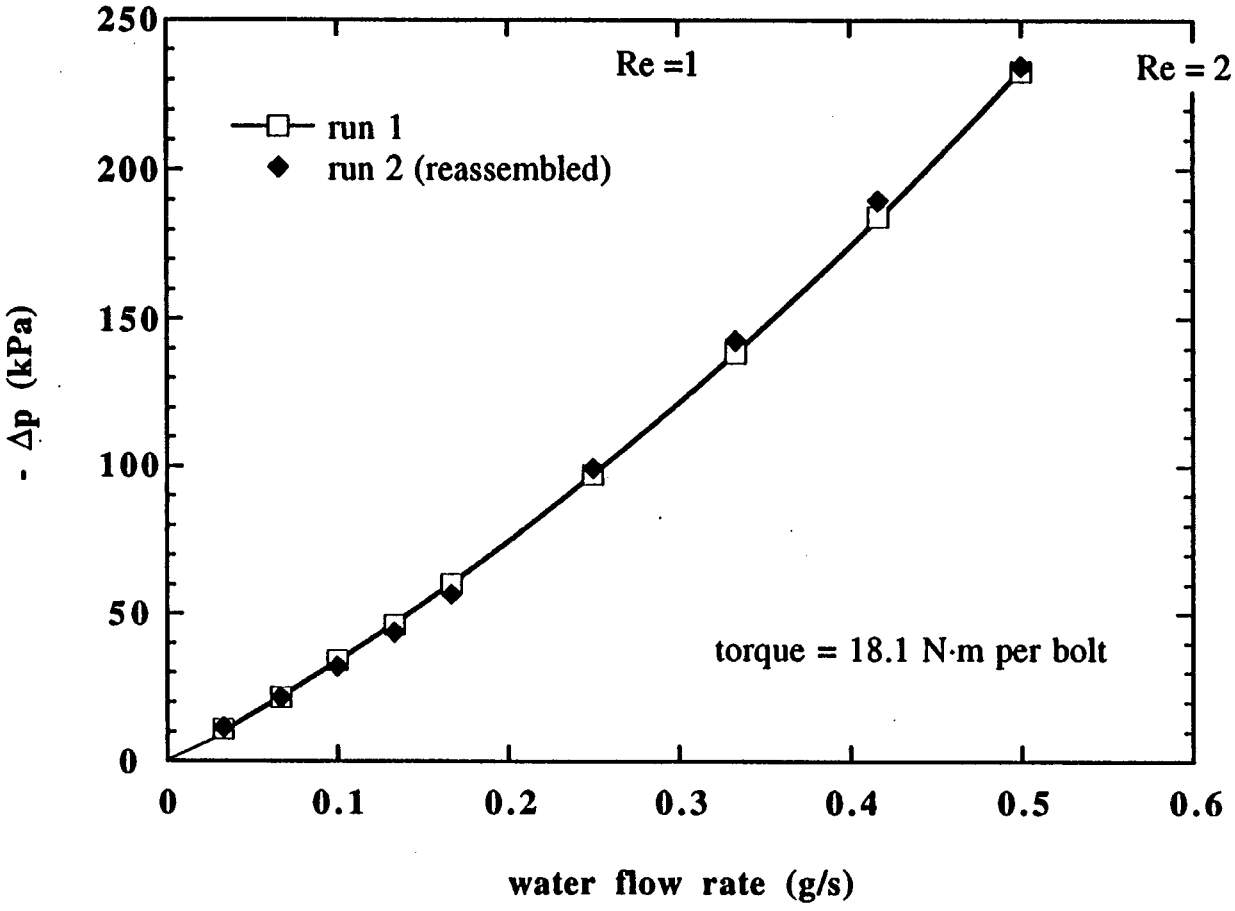

Fig. 3 Kovscek, Tretheway, Persoff, and Radke

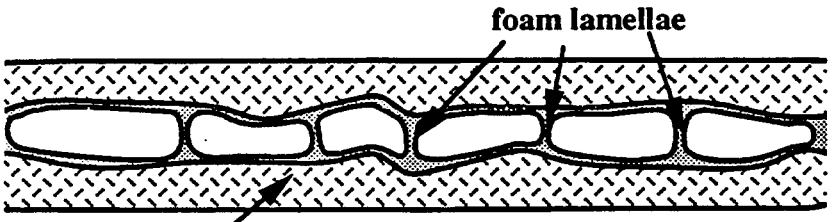

(a)

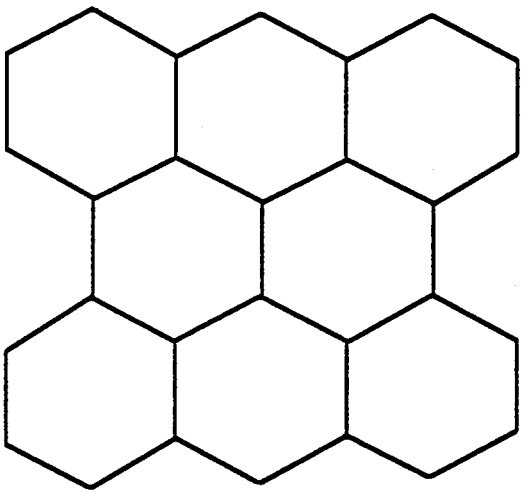

(b)

Fig. 4 Kovscek, Tretheway, Persoff, and Radke

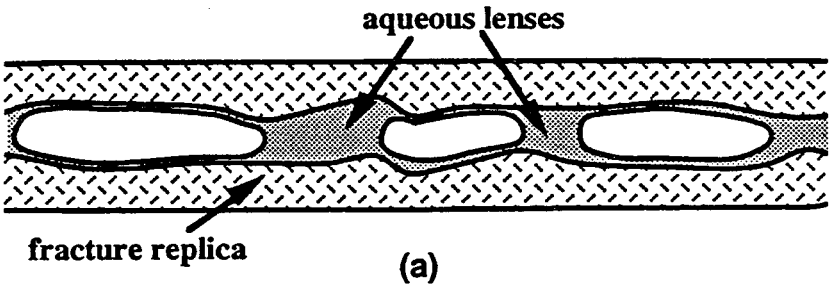

(a)

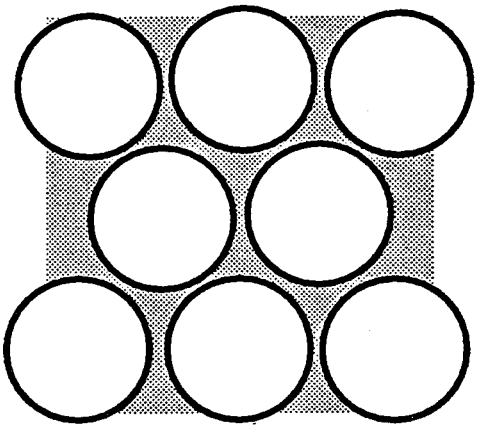

(b)

Fig. 5 Kovscek, Tretheway, Persoff, and Radke

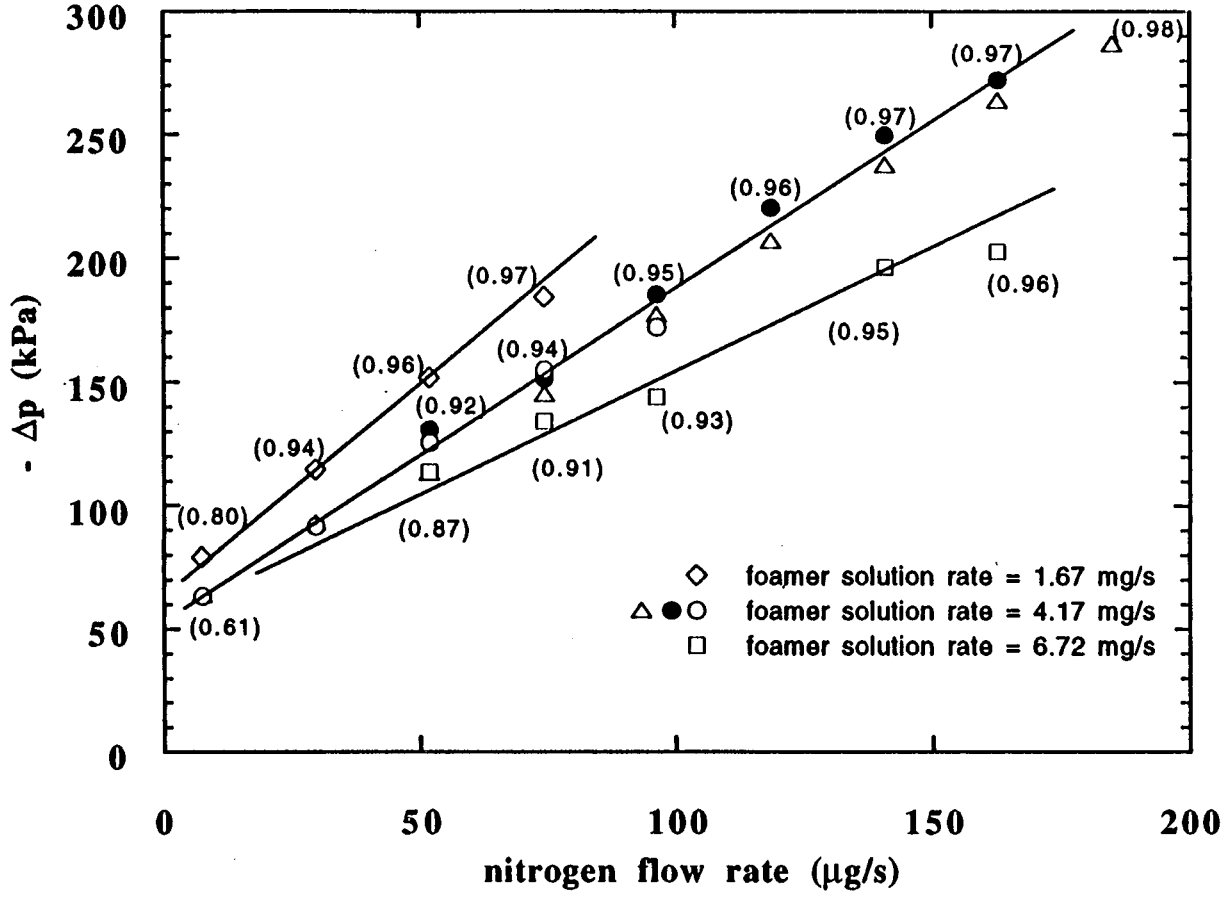

Fig .6 Kovscek, Tretheway, Persoff, and Radke

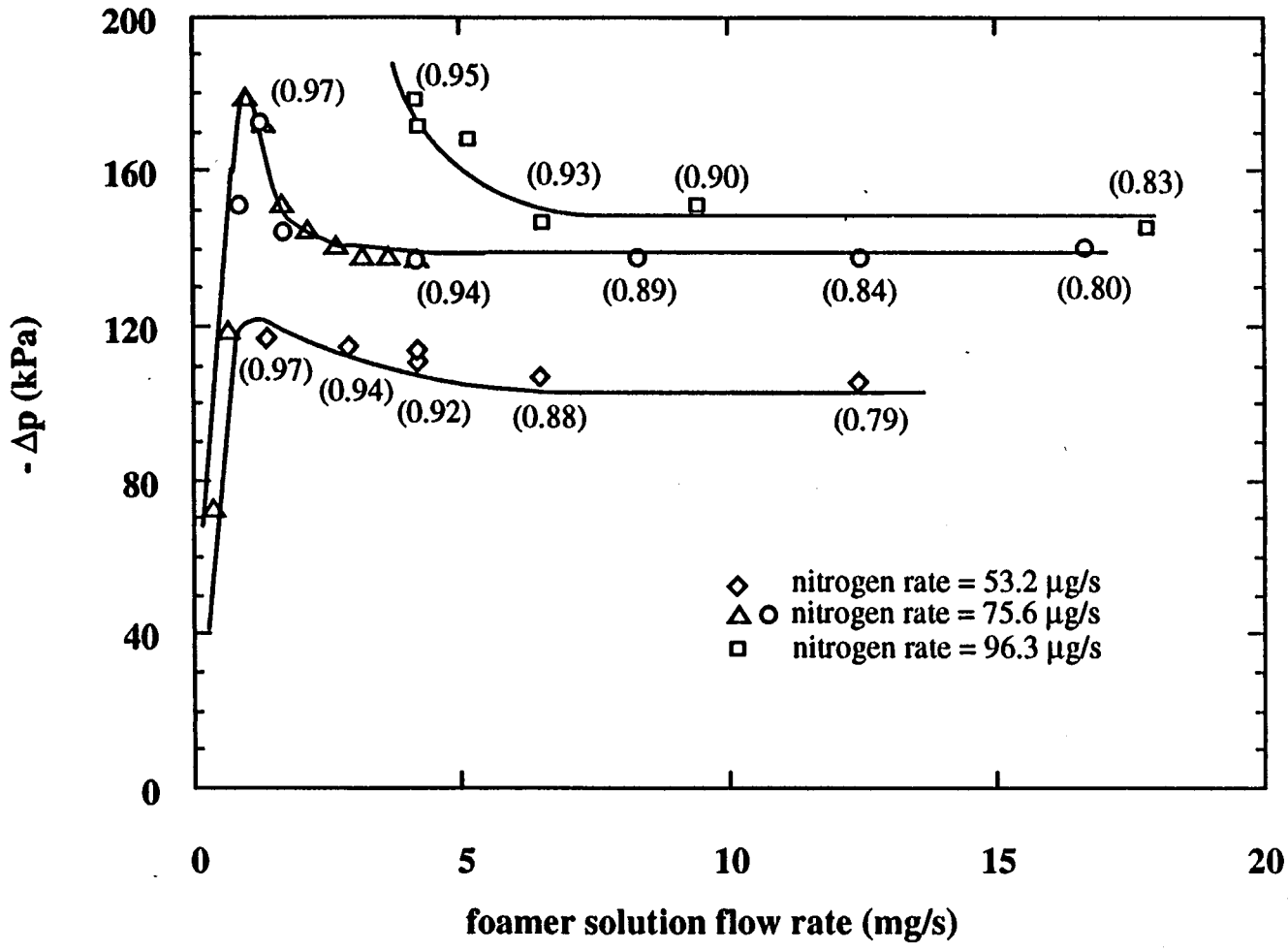

Fig. 7 Kovscek, Tretheway, Persoff, and Radke

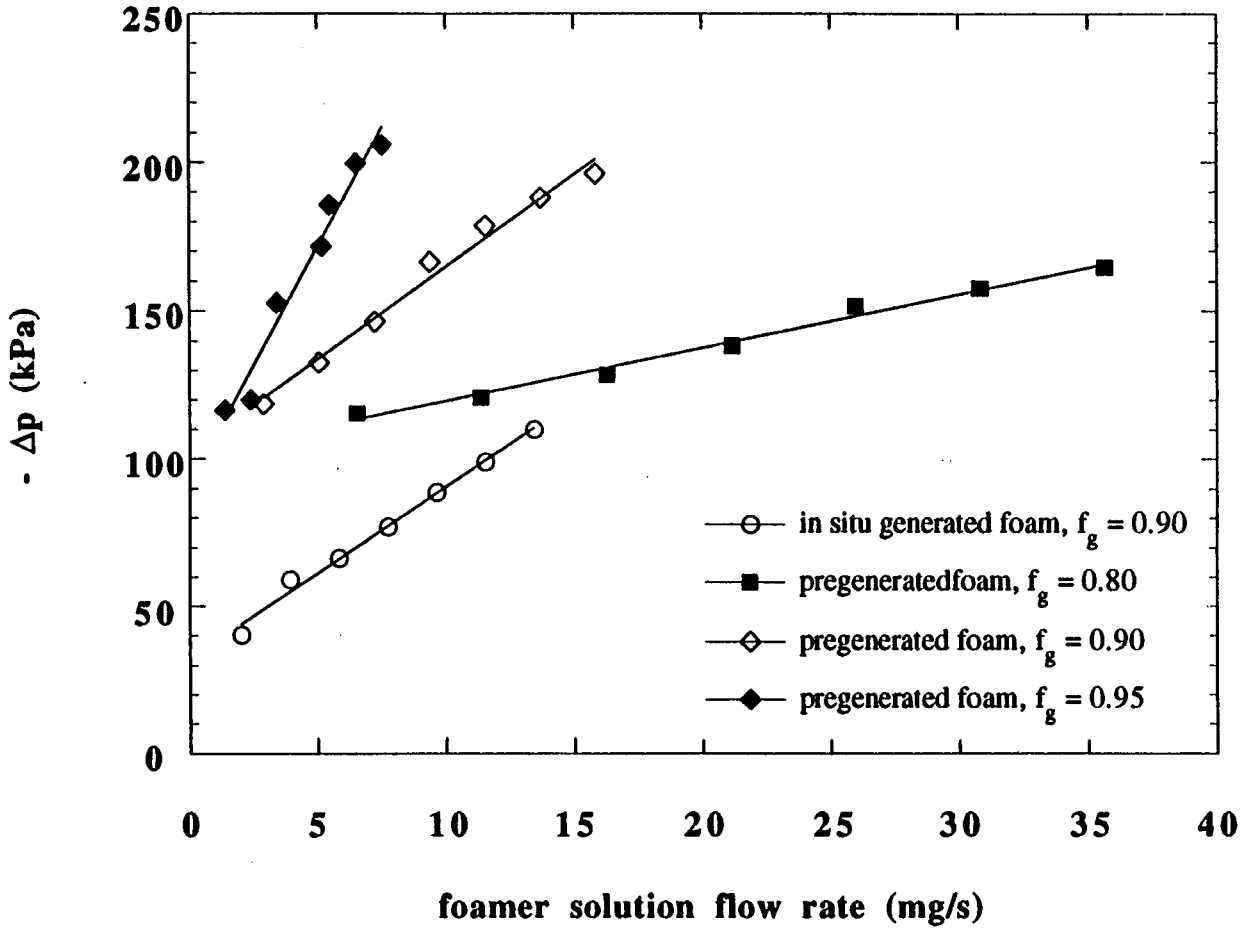

Fig. 8 Kovscek, Tretheway, Persoff, and Radke

☆U.S. GOVERNMENT PRINTING OFFICE: 1995 - 660-029/20043